Compensation of Zero-Current Clamping Effects in High-Frequency-Signal-Injection-Based Sensorless PM Motor Drives

Chan-Hee Choi, *Student Member, IEEE*, and Jul-Ki Seok, *Member, IEEE*

***Abstract*—This paper proposes an online compensation strategy for the unwanted disturbance voltage resulting from the zero-current clamping effect for high-frequency-signal-injection-based sensorless control schemes. We derive an analytical model that reveals intrinsic characteristics of the zero clamping effect for high-frequency signal injection. The model in this form is subsequently incorporated into the development of a specialized offline commissioning test to find motor inductances and a voltage distortion factor. From the sensitivity analysis of the effect on magnetic saturation, we confirm that the compensation error due to saturation has little negative impact on the proposed compensation method. The compensation result leads to an accurate position estimate in the zero-current clamping region. The proposed scheme does not rely on a complicated lookup table. Experiments demonstrate the superiority of the proposed method in suppressing the voltage distortions caused by the zero-current clamping effect.**

***Index Terms*—Analytical model, offline commissioning test, online compensation strategy for the unwanted disturbance voltage, zero-current clamping effect for high-frequency-signal-injection-based sensorless control.**

I. Introduction

A HIGH-FREQUENCY-signal-injection-based sensorless control scheme has recently drawn a great deal of interest as this scheme allows the achievement of the performance down to the zero stator frequency and parameter-independent position estimation [1]. This class of sensorless controller usually injects a revolving carrier-signal voltage vector to the motor using a voltage-source pulsewidth-modulation (PWM) inverter, which results in a carrier-signal current vector that can be used to estimate the rotor position. In practice, however, most of the early research often downplayed the presence of the PWM inverter deadtime at extremely low speeds. Indeed, because of the physical requirement, such inverter nonlinearities are always present in real plants [2]. An important issue relevant to inverter nonlinearity is the zero-current clamping that occurs when a phase current nears zero during the deadtime [3]–[5]. Only a few published works deal with this problem. In these works, there is the suggestion that its compensation is based on phase current information. It has been recently reported that the effect of zero-current clamping is a main contributor to a carrier-signal distortion in high-frequency-signal-injection-based sensorless control methods [6]–[8]. The common remedies for curing this problem have involved a complicated lookup table of experimental data [8]. This results in an immense engineering effort that is costly and time intensive. Therefore, this process may appear to be a time-consuming task even to a skilled engineer.

Another important issue relevant to the distortion of the carrier-signal current is the selection of carrier-signal voltage magnitude. Usually, a larger carrier-signal voltage is favored in order to achieve a better signal-to-noise ratio. When the signal injection-based sensorless control is used for a nonsalient permanent-magnet synchronous motor (PMSM) with very small magnetic saliency, for example, the superimposed voltage has a large value to amplify the small d–q axis impedance difference [9]. This may cause a relatively large carrier-signal current, which dominates over the very small fundamental current in a light load condition. This implies that the zero-current clamping region can be extended over the whole electrical angle of the phase current.

This paper demonstrates an online compensation method for the zero-current clamping effect of sensorless control schemes using a revolving carrier-signal. To fully explore the effects of zero-current clamping, the first step is usually the development of a mathematical model that faithfully represents the behavior of the physical phenomenon. The contribution presented in this paper is to introduce a formulation that systematically describes zero-current clamping effects for a carrier-signal component. Compensator design is also being pursued to achieve a higher level of performance. At the commissioning stage, a distortion factor with respect to zero-current clamping is obtained with the filtered high-frequency current and injection voltage command via offline. Then, the real-time compensation voltage is calculated from the distortion factor and the filtered high-frequency current. In contrast to previous work, the proposed strategy performs only one simple test without prior knowledge of deadtime and power device parameters. From the sensitivity analysis of the effect on magnetic saturation, we confirm that the estimation error resulting from saturation has little negative

Paper IPCSD-07-029, presented at the 2006 Industry Applications Society Annual Meeting, Tampa, FL, October 8–12, and approved for publication in the IEEE TRANSACTIONS ON INDUSTRY APPLICATIONS by the Industrial Drives Committee of the IEEE Industry Applications Society. Manuscript submitted for review October 31, 2006 and released for publication April 2, 2007. This work was supported by KESRI (R-2005-7-140), funded by the Ministry of Commerce, Industry, and Energy (MOCIE).

The authors are with the Power Conversion Laboratory, School of Electrical Engineering, Yeungnam University, Kyongsan 712-749, Korea (e-mail: doljk@ynu.ac.kr).

Color versions of one or more of the figures in this paper are available online at http://ieeexplore.ieee.org.

Digital Object Identifier 10.1109/TIA.2007.904409

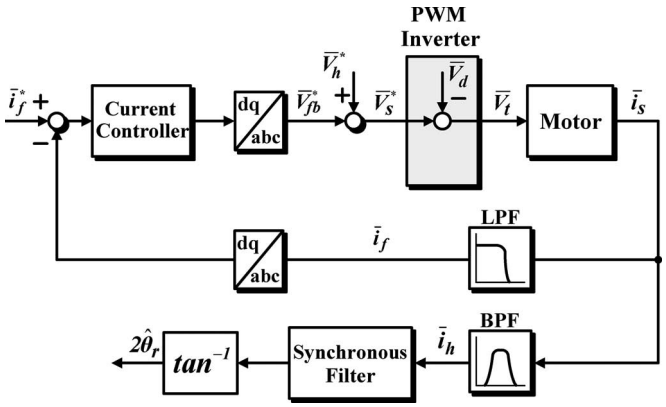

Fig. 1. Current control loop with disturbance voltage.

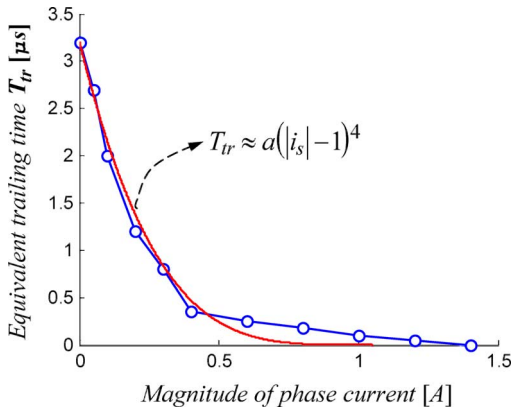

Fig. 2. Trajectory of $T_{\rm tr}$ around the zero-current region.

impact on the proposed compensation method. The developed algorithm has been implemented on a PMSM drive to confirm the effectiveness of the proposed scheme.

II. Modeling of the Zero-Current Clamping Effect

If the high-frequency voltage vector is superimposed on the fundamental excitation, the input–output voltage equation of a PWM inverter can be given by

$$\overline{V}_t = \overline{V}_s^* - \overline{V}_d = \overline{V}_{\rm fb}^* + \overline{V}_h^* - \overline{V}_d \tag{1}$$

where $\overline{V}_t$ is the motor terminal voltage vector, $\overline{V}_s^*$ indicates the command voltage vector, $\overline{V}_{\rm fb}^*$ is the current controller output voltage vector, and $\overline{V}_h^* (= V_h e^{j(\omega_c t + (\pi/2))})$ represents the injected voltage vector with a carrier frequency ω_c. $\overline{V}_d$ is the total disturbance voltage vector resulting from the inverter nonlinearity. The current control loop with the disturbance voltage is shown in Fig. 1.

The deadtime voltage error including the zero-current clamping effect has the following form in an arbitrary phase [3]:

$$V_d = \frac{T_{\rm cn} - T_{\rm tr}}{T_s} V_{\rm dc} {\rm sgn}(i_s) \tag{2}$$

where $T_{\rm tr}$ indicates an equivalent trailing time due to the parasitic capacitance of the insulated gate bipolar transistor (IGBT) around the zero-current region, T_s represents a sampling period, $V_{\rm dc}$ denotes a dc-link voltage, ${\rm sgn}(\cdot)$ denotes the sign function, and i_s is an instantaneous phase current. $T_{\rm cn}$ is an effective deadtime and can be represented as [2], [3]

$$T_{\rm cn} = T_d + t_{\rm on} - t_{\rm off} + \frac{V_{\rm on}}{V_{\rm dc}} T_s \tag{3}$$

where T_d indicates a nominal interlock time, $t_{\rm on}/t_{\rm off}$ represent the turn-on/turn-off time, and $V_{\rm on}$ is an average ON-state voltage of the power device.

In practice, a rising/falling time of the output voltage pulse significantly increases to charge the parasitic capacitance as the current is close to zero [3]–[5]. When the rising/falling time is longer than $T_{\rm cn}$, however, the actual trailing time cannot exceed the effective deadtime [3], [4]. When the deadtime expires, for instance, the turn-on of the low IGBT makes the upper parasitic capacitor be immediately charged since the lower IGBT provides a low resistance path. Here, the equivalent trailing time represents the actual trailing time limited by the effective deadtime around the zero-current region. It has the following relationship with the compensation time T_c which can reject the voltage distortion of (2):

$$T_c = T_{\rm cn} - T_{\rm tr}. \tag{4}$$

Fig. 2 shows the typical trajectory of $T_{\rm tr}$ with the current amplitude which can be reconstructed using stored experimental data. Since the trajectory is always bounded within the effective deadtime near the zero-current point and decrease as the current increases, the outlines of $T_{\rm tr}$ have the roughly identical shape irrespective of the device rating or its manufacturer [4]. The nonlinear trajectory can be approximated by a polynomial of low degree, as shown by (5) at the bottom of the page, where $a = T_{\rm cn} = 3.2 \times 10^{-6}$. When the machine is fed by a voltage vector with a high-frequency excitation, a general expression of an instantaneous phase current in an arbitrary phase will be of the following form:

$$i_s = i_f + i_h \tag{6}$$

where i_f represents a fundamental current component, and i_h is a resulting carrier-signal current. Substituting (5) into (2) becomes

$$V_d = \begin{cases} \frac{T_{\rm cn} - T_{\rm cn}(i_s - 1)^4}{T_s} V_{\rm dc}, & \text{if } 0 \le i_s < 1 \\ \frac{-T_{\rm cn} + T_{\rm cn}(i_s + 1)^4}{T_s} V_{\rm dc}, & \text{if } -1 < i_s < 0 \end{cases}. \tag{7}$$

$$T_{\rm tr} \approx \begin{cases} a\left(|i_s| - 1\right)^4 = a\left(|i_s|^4 - 4|i_s|^3 + 6|i_s|^2 - 4|i_s| + 1\right), & \text{if } |i_s| < 1 \\ 0, & \text{if } |i_s| \ge 1 \end{cases} \tag{5}$$

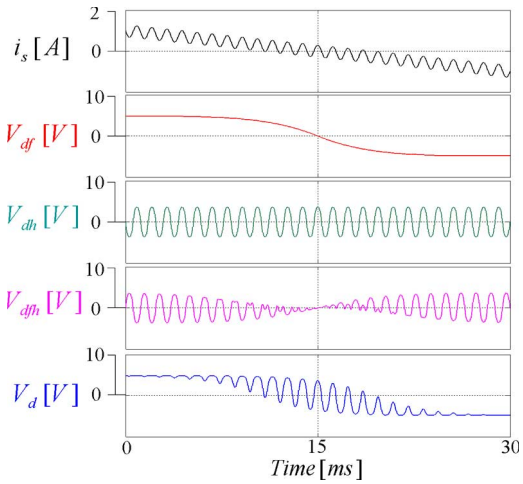

Fig. 3. Phase current and calculated disturbance voltage.

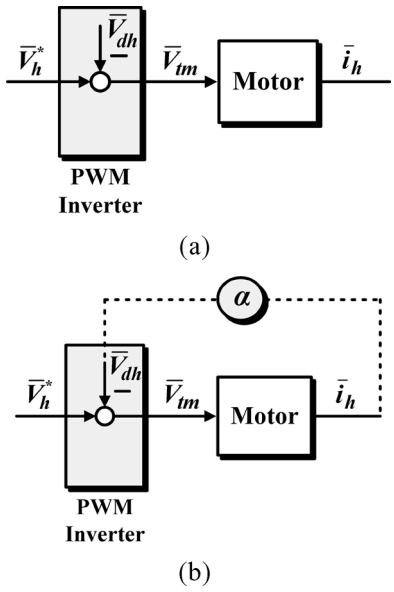

Fig. 4. Inverter model for high-frequency components. (a) Open-loop model. (b) Closed-loop model considering the zero-current clamping effect.

By combining (6) and (7), the total disturbance voltage V_d can be described by

$$V_d = V_{\rm df}(i_f) + V_{\rm dh}(i_h) + V_{\rm dfh}(i_f, i_h) \tag{8}$$

where $V_{\rm df}$, $V_{\rm dh}$, and $V_{\rm dfh}$ are defined in (9a)–(9c), as shown at the bottom of the page.

In (8), and (9a)–(9c), $V_{\rm df}$ indicates the disturbance voltage resulting from the fundamental component, $V_{\rm dh}$ denotes the disturbance voltage due to the carrier-signal component, and $V_{\rm dfh}$ is the coupling voltage resulting from the interaction between the fundamental and high-frequency signal.

Fig. 3 shows the phase current waveform and the calculated disturbance voltage plots using (8), and (9a)–(9c) while i_f is changed from -1 to 1 A, and i_h with 0.3 A–850 Hz has been superimposed. It is possible to observe that the amplitude-modulated coupling term $V_{\rm dfh}$ is in antiphase to $V_{\rm dh}$ and its maximum is found around $|i_s| = 1$. This feature allows the total disturbance voltage V_d to be always limited by the effective deadtime voltage. This is consistent with the fact that the actual trailing time cannot exceed the effective deadtime.

Naturally, the effect of $\overline{V}_{\rm dh}$ fully appears in the vicinity of the zero-current region. Neglecting the higher order terms of (9b) because the voltage distortion centers around the region less than 0.5 A, as illustrated in Fig. 2, $\overline{V}_{\rm dh}$ can be expressed using the periodic carrier-signal current vector $\bar{i}_h$ as

$$\overline{V}_{\rm dh} \cong \alpha \bar{i}_h. \tag{10}$$

It is found from (10) and Fig. 3 that $\overline{V}_{\rm dh}$ is of the same carrier frequency and in phase with the high-frequency current. The constant α represents a distortion factor which depends on the switching device parameters and a dc-link voltage. Thus, the zero-current clamping effect for the high-frequency component can be modeled, as shown in Fig. 4(b), while the high-frequency voltage is injected into the machine in open loop. In this figure, $\overline{V}_{\rm tm}$ is the inverter output voltage for the high-frequency component.

If ω_c is much larger than the fundamental excitation frequency, then a carrier-signal current–voltage model around the zero-current region is given by

$$\bar{i}_h = \frac{V_h e^{j\left(\omega_c t + \frac{\pi}{2}\right)}}{\overline{L}_s p + \alpha} \tag{11}$$

where $\overline{L}_s$ is the stator inductance matrix with a position saliency, and p indicates a differential operator. It is seen that

$$V_{\rm df} = \begin{cases} \frac{T_{\rm cn} - T_{\rm cn}(i_f - 1)^4}{T_s} V_{\rm dc}, & \text{if } 0 \le i_f < 1 \\ \frac{-T_{\rm cn} + T_{\rm cn}(i_f + 1)^4}{T_s} V_{\rm dc}, & \text{if } -1 < i_f < 0 \end{cases} \tag{9a}$$

$$V_{\rm dh} = \begin{cases} \frac{T_{\rm cn} - T_{\rm cn}(i_h - 1)^4}{T_s} V_{\rm dc}, & \text{if } 0 \le i_h < 1 \\ \frac{-T_{\rm cn} + T_{\rm cn}(i_h + 1)^4}{T_s} V_{\rm dc}, & \text{if } -1 < i_h < 0 \end{cases} \tag{9b}$$

$$V_{\rm dfh} = \begin{cases} \frac{-T_{\rm cn}\left(4i_f^3 i_h - 12 i_f^2 i_h + 6 i_f^2 i_h^2 + 12 i_f i_h - 12 i_f i_h^2 + 4 i_f i_h^3\right)}{T_s} V_{\rm dc}, & \text{if } 0 \le i_s < 1 \\ \frac{T_{\rm cn}\left(4i_f^3 i_h + 12 i_f^2 i_h + 6 i_f^2 i_h^2 + 12 i_f i_h + 12 i_f i_h^2 + 4 i_f i_h^3\right)}{T_s} V_{\rm dc}, & \text{if } -1 < i_s < 0 \end{cases} \tag{9c}$$

the distortion factor acts like a nonlinear resistance which appears in every zero-current clamping region. An inspection of (10) and (11) shows that the nonzero α introduces a distortion in terms of magnitude and phase of the carrier-signal current. Apparently, the distortion of the carrier-signal current containing the position information significantly affects the quality of the position estimate.

III. Proposed Compensation Strategy

The carrier-signal current–voltage model (11) is taken as the starting point of the proposed online compensation strategy. Here, an accurate acquisition of α is a major concern for the estimation of $\overline{V}_{\rm dh}$.

In steady state, the denominator of (11) can be rewritten in (12), as shown at the bottom of the page, where θ_r indicates the rotor position, L_s is the average stator inductance, and ΔL_s is the differential stator inductance [10].

Hence, the d- and q-axes carrier-signal currents are given as

$$i_{\rm dsh} = \frac{-j\omega_c L_s \sin\omega_c t + j\omega_c \Delta L_s \sin(2\theta_r - \omega_c t) - \alpha \sin\omega_c t}{\alpha^2 - \omega_c^2 (L_s^2 - \Delta L_s^2) + j\omega_c 2\alpha L_s} V_h \tag{13a}$$

$$i_{\rm qsh} = \frac{j\omega_c L_s \cos\omega_c t - j\omega_c \Delta L_s \cos(2\theta_r - \omega_c t) + \alpha \cos\omega_c t}{\alpha^2 - \omega_c^2 (L_s^2 - \Delta L_s^2) + j\omega_c 2\alpha L_s} V_h. \tag{13b}$$

From (13), notice that the most significant factor which influences the α estimation is the value of stator inductances. An accurate estimation of α in the model is critical for the success of the following compensator design. In this paper, we propose an offline commissioning process to decide L_s and ΔL_s prior to start-up.

A. Offline Commissioning Procedure

To alleviate the need for a real position sensor, we next consider a no-load commissioning test that requires only the information of the fundamental current position. An example is shown in Fig. 5, depicting the d-axis filtered fundamental current $i_{\rm dsf}$ and carrier-signal current $i_{\rm dsh}$ in the stationary coordinate for a PMSM at 100 r/min driven by a 600-W inverter with a deadtime of 3.5 μs and without any deadtime compensation. In this paper, the d-axis fundamental current of 2 A in a synchronous coordinate is intentionally added to observe the distortion region resulting from the zero-current clamping effect. Significant distortion in $i_{\rm dsh}$ appears at 30° and 90° region. This distortion is correlated to the zero-crossing position of motor fundamental currents. At no-load, the generated net torque is zero and the actual rotor angle is still synchronized to the fundamental current position. This means that the whole process can be carried out without any real position sensor at a given test condition. In contrast, no distortion is observed around 0° or the peak region where the carrier-signal current–voltage model is

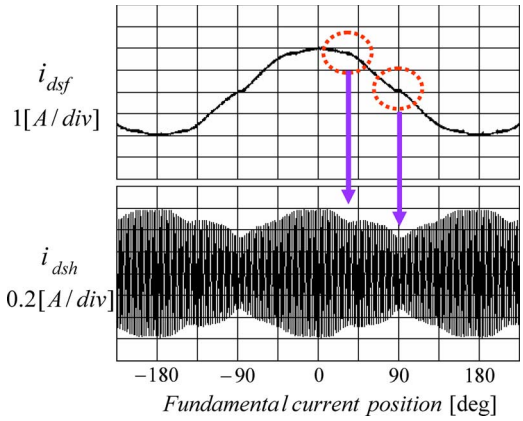

Fig. 5. Zero-current clamping effect of the fundamental current and the carrier-signal current.

$$\bar{i}_h = \frac{V_h e^{j\left(\omega_c t + \frac{\pi}{2}\right)}}{\overline{L}_s p}. \tag{14}$$

Capturing the d- and q-axes carrier-signal currents in the peak region of the phase current, the stator inductance can be obtained from (14) as

$$\hat{L}_s = \frac{V_h}{2\omega_c}\left(\frac{1}{i_{\rm dsh}|_{0^\circ}} + \frac{1}{i_{\rm qsh}|_{0^\circ}}\right) \tag{15a}$$

$$\Delta\hat{L}_s = \frac{V_h}{2\omega_c}\left(-\frac{1}{i_{\rm dsh}|_{0^\circ}} + \frac{1}{i_{\rm qsh}|_{0^\circ}}\right) \tag{15b}$$

where $i_h|_{0^\circ}$ is the carrier-signal current amplitude at the peak point of the fundamental current. In the zero-crossing region, the amplitude of the measured d-axis carrier-signal current of (13a) is

$$i_{\rm dsh}|_{\pm 90^\circ} = V_h \frac{-\sin\omega_c t\left(j\omega_c(\hat{L}_s - \Delta\hat{L}_s) + \alpha\right)}{\alpha^2 - \omega_c^2\left(\hat{L}_s^2 - \Delta\hat{L}_s^2\right) + j\omega_c 2\alpha\hat{L}_s} \tag{16}$$

where $i_h|_{\pm 90^\circ}$ is the carrier-signal current amplitude at the zero crossing of the fundamental current.

$$\overline{L}_s p + \alpha = \begin{bmatrix} j\omega_c(L_s - \Delta L_s \cos 2\theta_r) + \alpha & -j\omega_c \Delta L_s \sin 2\theta_r \\ -j\omega_c \Delta L_s \sin 2\theta_r & j\omega_c(L_s + \Delta L_s \cos 2\theta_r) + \alpha \end{bmatrix} \tag{12}$$

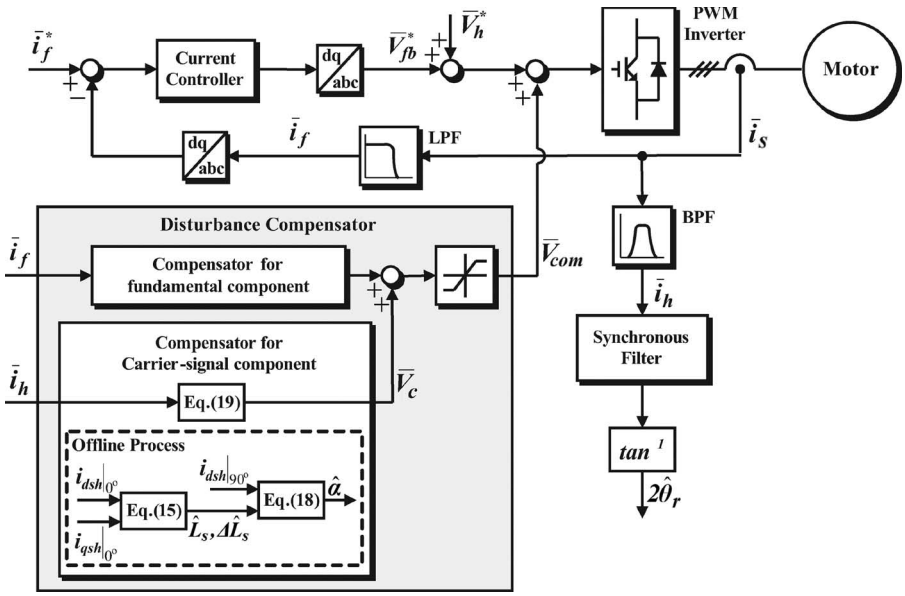

Fig. 6. Proposed disturbance voltage compensation scheme.

The maximum amplitude occurs when $\omega_c t = -90^\circ$ and can be written as

$$i_{\mathrm{dsh\_}m}|_{\pm 90^\circ} = \frac{V_h\sqrt{\alpha^2 + \left\{\omega_c(\hat{L}_s - \Delta\hat{L}_s)\right\}^2}}{\sqrt{\left\{\omega_c^2\left(\hat{L}_s^2 - \Delta\hat{L}_s^2\right) - \alpha^2\right\}^2 + (2\omega_c\alpha\hat{L}_s)^2}}. \tag{17}$$

From (17), therefore, the distortion factor is obtained as

$$\hat{\alpha} = \sqrt{\left(\frac{V_h}{i_{\mathrm{dsh\_}m}|_{\pm 90^\circ}}\right)^2 - \omega_c^2(\hat{L}_s + \Delta\hat{L}_s)^2}. \tag{18}$$

The distortion factor α is obtained from the offline identification process and retrieved online to reconstruct the compensation voltage that fits the actual operating point. Then, the online compensation voltage vector can be simply obtained from (10) and (11) as

$$\overline{V}_c = \hat{\alpha}\bar{i}_h. \tag{19}$$

This means that the online compensation algorithm looks very promising to relieve the computation burden. This makes the proposed algorithm very useful for real-time applications. Fig. 6 shows the overall block diagram of the disturbance compensation strategy. In real implementation, the compensation voltage is limited by the value of the effective deadtime voltage.

B. Sensitivity of Distortion Factor on Magnetic Saturation Effect

In practice, the inductance is estimated around the peak point of the phase current as (15a) and (15b). However, the distortion factor calculation using the estimated inductance is performed at the zero crossing of the phase current. This means that the acquisition of α would be affected by the magnetic saturation due to the amplitude difference of the fundamental

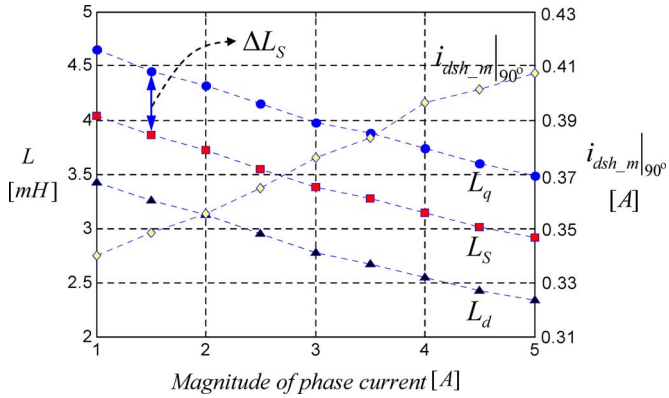

Fig. 7. Variation of inductances and carrier-signal current versus phase current.

current. Therefore, the effect of the magnetic saturation on the α identification will be investigated in this paper.

The fundamental current amplitude to be selected should be large enough to find the region satisfying the condition of (14). The increase of the fundamental current simultaneously leads to the reduction of the d- and q-axes inductance value [11]. Naturally, this reduction results in an amplitude increase of the carrier-signal current since the fixed voltage is injected. In other words, from (11) and (14), the decrease of the inductance value resulting from saturation boosts the carrier-signal current amplitude. This implies that the $\bar{i}_h$-to-$\overline{L}_s$ ratio with respect to the phase current amplitude is maintained at a constant level. Hence, the distortion factor of (11) is not mutually interfered with by the magnetic saturation effect. It is worth mentioning that the proposed estimation accuracy is very robust to the magnetic saturation effect.

Fig. 7 shows the measured inductance trajectory and the maximum amplitude curve of the measured d-axis carrier-signal current using (15a), (15b), and (17) for a varied phase current spread over a range of approximately the rated motor current. Due to the uniform saturation effect occurring on the

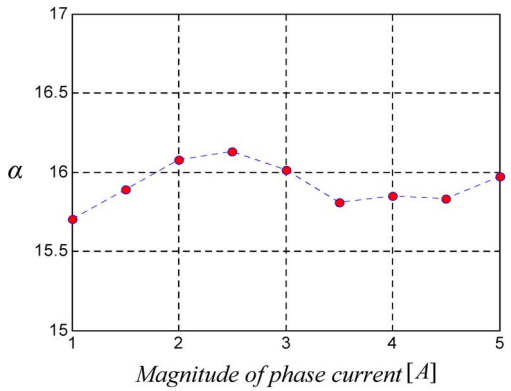

Fig. 8. Distortion factor sensitivity on the magnetic saturation.

TABLE I
RATINGS AND KNOWN PARAMETER OF PMSM UNDER TEST

Rating and Parameter	Value	Unit
Rated power output	600	W
Rated current	5.1	A_{peak}
Rated speed	3000	r/min
Number of pole pairs	4	poles
Stator Resistance	0.714	Ω
Stator Inductance	4.59	mH

d- and q-axes, L_s drifts at a rate equal to the rate of the d- and q-axes inductance attenuation, whereas ΔL_s is almost flat. As mentioned before, it is seen that the decreased inductances boost the carrier-signal current. The distortion factor can be obtained from (18). The test result is plotted in Fig. 8. Although the inductance considerably varies, as shown in Fig. 7, the maximum fluctuation range of α is bounded within $\pm 1.5\%$. Therefore, it is evident that the proposed identification process can be extended to other types of machines only if a machine is roughly subjected to the saturation trend of Fig. 7.

IV. EXPERIMENTAL RESULTS

The proposed algorithm is implemented on a commercial 600-W PMSM described in Table I. The PWM inverter is constructed in the laboratory using 10-kHz switching Semikron SKM 75GB IGBT modules, and the nominal interlock time T_d is 3.5 μs. Two-phase currents are sampled with a rate of 50 μs, and the fundamental current regulator is tuned for a 1500 rad/s bandwidth. The injection condition has been set to 10 V–850 Hz through a tuning process. In this paper, the injection voltage/hertz is adjusted to achieve the desired position saliency in the resulting carrier-signal current by iterative manual tests. The rotor position estimation is obtained through a signal processing method using bandpass filters and low-pass filters. The test parameters are summarized in Table II.

In a practical digital implementation, there would be the inherent time delay between the actual disturbance voltage and the compensation voltage. The corresponding delay time is converted to the phase lag, which can influence the compensation quality. It is found that the compensation performance is everworsening as the phase lag widens and almost reaches one without compensation when the phase lag exceeds 90°.

TABLE II
OPERATING PARAMETERS OF IMPLEMENTED DRIVE

Parameter	Value	Unit
DC-Link Voltage	200	V
Sampling Period	50	μs
Injection Voltage	10	V
Injection Frequency	850	Hz

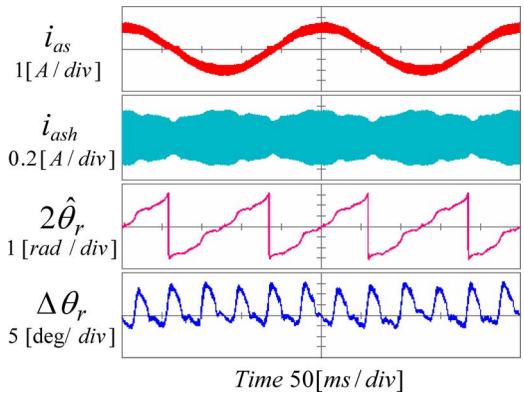

Fig. 9. Test result without any compensation.

The first step in the offline commissioning stage is to acquire filtered carrier-signal currents and find inductance values. In this process, the filtered current data were captured at 100 r/min without any compensation. The d-axis current is set to 2 A. Then, the distortion factor is obtained and fixed as 16.1 in all tests. All the procedures for the offline commissioning can be performed using a local computer. This computer is commonly connected to the motor drive system as a host controller.

Fig. 9 shows time-domain responses without any deadtime compensation when the sensor-controlled motor is running at 60 r/min. From the top, the A-phase current, the bandpass filtered carrier-signal current, the estimated position, and the position error are depicted. It can be seen that a significant distortion is evident in the carrier-signal current envelope when the phase currents are close to zero. Such distortions lead to visible perturbations in the position error at six times the fundamental frequency. The spike ripple in the position error has a direct impact on the quality of the sensorless control performance.

The same experiment under the fundamental current compensation alone is repeated, as shown in Fig. 10. In this test, the compensation scheme of $\overline{V}_{\mathrm{df}}$ is based on that of [12]. Although the compensation on the fundamental current is performed, significant ripples are still observed in the position error waveform. This implies that the carrier-signal current compensation is much more effective to reduce the position error ripple than the fundamental current compensation. This is explained by the fact that the estimated position is determined by processing the carrier-signal current, not by the fundamental current.

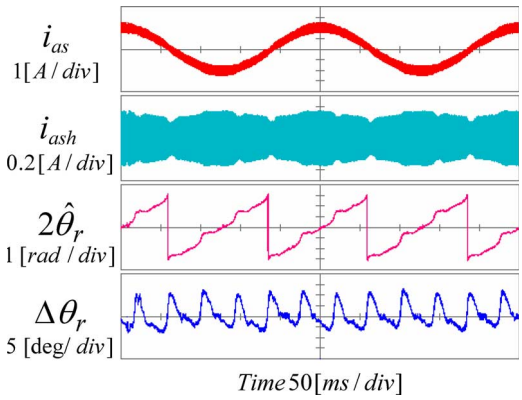

Fig. 10. Test result with the fundamental current compensation alone.

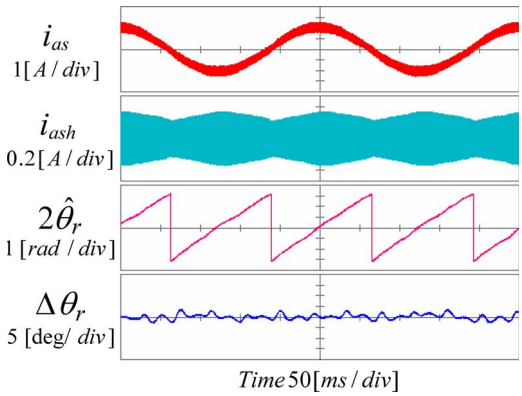

Fig. 11. Compensation result of the proposed scheme.

Fig. 11 shows the performance of the proposed zero-current clamping compensation scheme. The estimated compensation voltage is added to the overall input to cancel the effect of the nonlinear disturbance with a feedforward manner, as depicted in Fig. 6. In the carrier-signal current plot, the desired rotor-position-dependent saliency is clearly visible. The residual distortion is mainly the results of the stator tooth effect, the current measurement error, and the digital implementation. Compared to the case without compensation, a close inspection of the position error plot shows that the maximum amplitude greatly reduced to less than ± 5 electrical degrees. Combining the proposed compensator with the offline commissioning identification yields a 70% improvement of the root-mean-square position error over the fundamental current compensation alone. It is concluded that the proposed algorithm can provide reliable compensation performance in a real situation without a complicated lookup table. This can never be achieved in other inverter nonlinearity compensation schemes.

Fig. 12 shows a plot where the phase current is intentionally increased up to the rated current to assess the compensation performance under magnetic saturation. Other conditions are the same as those of Fig. 11. Although strong saturation exists in the motor, the carrier-signal current still provides the smooth envelope containing the spatial saliency. The position error response seems to be more improved but this is because of the shorter zero crossing of the fundamental current. The result shows a good agreement with the analysis of the magnetic saturation effect.

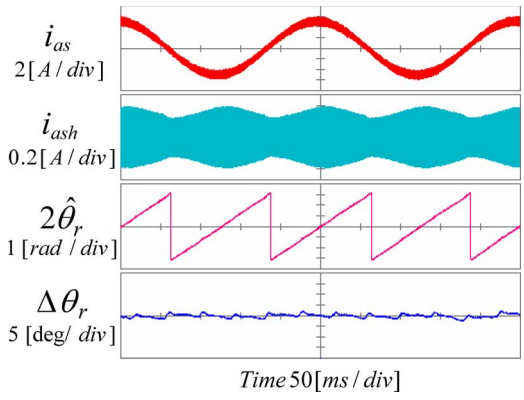

Fig. 12. Compensation result of the proposed scheme under the rated current condition.

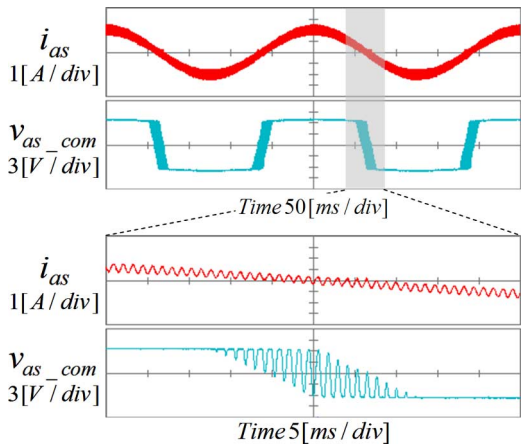

Fig. 13. Phase current and compensation voltage of the proposed scheme.

The two upper plots of Fig. 13 depict the A-phase current and the compensation voltage which represents the suppression voltage for the total disturbance effect. The shaded portion of the upper waveform is enlarged in the lower side, showing that the compensation voltage is of the same carrier frequency and in phase with the carrier-signal current. The final compensation voltage is always limited by the effective deadtime voltage because the actual trailing time cannot exceed the effective deadtime. A very close match is found between the calculated V_d in Fig. 3 and the compensation voltage. In the magnified current plot, the magnitude and phase distortion in the carrier signal are rarely found even when the phase current crosses to zero.

This means that the proposed method effectively compensates for distortions due to the zero-current clamping in the high-frequency-signal-injection-based sensorless control without requiring any iterative manual tunings and/or lookup tables.

V. Conclusion

This paper has described a proposal for a model-based compensation method for the disturbance voltage resulting from zero-current clamping in high-frequency-signal-injection-based sensorless control. Specifically, an analytical model has been presented, which accurately modeled the behavior of the

zero-clamping effect for a high-frequency signal. The proposed compensation design has greatly reduced the commissioning effort to build the lookup table [8], while achieving comparable performance as the fully calibrated lookup-table-based compensator does [8]. Extensive test results have showed that the proposed scheme exhibited considerable robustness with respect to the magnetic saturation effect and a performance improvement even in the absence of device parameter information.

REFERENCES

[1] J. Holtz, "Sensorless control of induction machines—With or without signal injection," *IEEE Trans. Ind. Electron.*, vol. 53, no. 1, pp. 7–30, Dec. 2006.

[2] J. W. Choi and S. K. Sul, "Inverter output voltage synthesis using novel dead time compensation," *IEEE Trans. Power Electron.*, vol. 11, no. 2, pp. 221–227, Mar. 1996.

[3] N. Urasaki, T. Senjyu, T. Kinjo, T. Funabashi, and H. Sekine, "Dead-time compensation strategy for permanent magnet synchronous motor drive taking zero-current clamp and parasitic capacitance effects into account," *Proc. Inst. Electr. Eng.—Electr. Power Appl.*, vol. 152, no. 4, pp. 845–853, Jul. 2005.

[4] J. S. Kim, J. W. Choi, and S. K. Sul, "Analysis and compensation of voltage distortion by zero current clamping in voltage-fed PWM inverter," *Trans. Inst. Electr. Eng. Jpn.*, vol. 117-D, no. 2, pp. 160–165, Feb. 1997.

[5] R. B. Sepe and J. H. Lang, "Inverter nonlinearities and discrete-time vector current control," *IEEE Trans. Ind. Appl.*, vol. 30, no. 1, pp. 62–70, Jan./Feb. 1994.

[6] C. Silva, G. M. Asher, and M. Sumner, "Influence of dead-time compensation on rotor position estimation in surface mounted PM machines using HF voltage injection," in *Proc. IEEE Power Conversion Conf.*, Osaka, Japan, 2002, pp. 1279–1284.

[7] J. M. Guerrero, M. Leetmaa, F. Briz, A. Zamarron, and R. D. Lorenz, " Inverter nonlinearity effects in high-frequency signal-injection-based sensorless control methods," *IEEE Trans. Ind. Appl.*, vol. 41, no. 2, pp. 618–626, Mar./Apr. 2005.

[8] N. Teske, G. M. Asher, M. Sumner, and K. J. Bradley, "Analysis and suppression of high-frequency inverter modulation in sensorless position-controlled induction machine drives," *IEEE Trans. Ind. Appl.*, vol. 39, no. 1, pp. 10–18, Jan./Feb. 2003.

[9] J. H. Jang, J. I. Ha, M. Ohto, K. Ide, and S. K. Sul, "Analysis of permanent-magnet machine for sensorless control based on high-frequency signal injection," *IEEE Trans. Ind. Appl.*, vol. 40, no. 6, pp. 1595–1604, Nov./Dec. 2004.

[10] M. W. Degner and R. D. Lorenz, "Using multiple saliencies for the estimation of flux, position, and velocity in AC machines," *IEEE Trans. Ind. Appl.*, vol. 34, no. 5, pp. 1097–1104, Sep./Oct. 1998.

[11] J. H. Jang, S. K. Sul, J. I. Ha, K. Ide, and M. Sawamura, "Sensorless drive of surface-mounted permanent-magnet motor by high-frequency signal injection based on magnetic saliency," *IEEE Trans. Ind. Appl.*, vol. 39, no. 4, pp. 1031–1039, Jul./Aug. 2003.

[12] C. H. Choi, K. R. Cho, and J. K. Seok, "Inverter nonlinearity compensation in the presence of current measurement errors and switching device parameter uncertainties," *IEEE Trans. Power Electron.*, vol. 22, no. 2, pp. 576–583, Mar. 2007.

Chan-Hee Choi (S'06) received the B.S. and M.S. degrees in electrical engineering from Yeungnam University, Kyongsan, Korea, in 2004 and 2007, respectively, where he is currently working toward the Ph.D. degree in the Power Conversion Laboratory, School of Electrical Engineering.

His current research interests include high-performance electrical machine drives and sensorless drives of ac machine.

Jul-Ki Seok (S'94–M'98) received the B.S., M.S., and Ph.D. degrees from Seoul National University, Seoul, Korea, in 1992, 1994, and 1998, respectively, all in electrical engineering.

From 1998 to 2001, he was a Senior Engineer with the Production Engineering Center, Samsung Electronics, Suwon, Korea. Since 2001, he has been with the Power Conversion Laboratory, School of Electrical Engineering, Yeungnam University, Kyongsan, Korea, where he is currently an Associate Professor. His current research interests include high-performance electrical machine drives, sensorless control of ac machines, and nonlinear system identification related to the power electronics field.